Dalton Transactions

ROYAL SOCIETY OF CHEMISTRY

PAPER

View Article Online
View Journal

Cite this: DOI: 10.1039/d5dt02965a

Structure–performance relationship in copper phthalocyanine-based supercapacitor electrodes: influence of substituent geometry from molecular design to electrochemical function

Şirin Siyahjani-Gültekin, *[a] Berivan Arin Öztürmen,[b] Damla Şahin,[a] Gülşah Yilmaz,[a] Bahar Tosun Ercan,[a] Burak Gültekin [a] and Zekeriya Biyiklioglu *[b]

This work investigates how the substituent position governs the structure–performance relationship of copper phthalocyanine (CuPc) derivatives used as supercapacitor electrodes. Two positional isomers bearing the same (3,4,5-trimethoxybenzyl)oxy substituent, namely the peripheral derivative (**TMe-Cu**) and the non-peripheral derivative (**n-TMe-Cu**), were synthesized and characterized by spectroscopic and structural techniques. Electrochemical evaluation in 1 M H_2SO_4 using cyclic voltammetry, galvanostatic charge–discharge, electrochemical impedance spectroscopy, and scan-rate-dependent kinetic analyses revealed a pronounced performance advantage for **n-TMe-Cu**, which delivered a specific capacitance of up to 360 F g^{-1} at 1 A g^{-1} and retained 80% of its initial capacitance after 5000 cycles. Dunn analysis showed that **n-TMe-Cu** exhibits a substantially higher surface-controlled contribution than **TMe-Cu**, indicating that a larger fraction of charge storage proceeds through rapidly accessible interfacial pathways. In conjunction with the observed morphological differences between the two electrodes, these results suggest that non-peripheral substitution promotes a more electrochemically accessible electrode architecture and more favourable charge-storage kinetics. Overall, this study demonstrates that substituent geometry is a key molecular design parameter for regulating electrochemical utilization and rate performance in CuPc-based organic electrode materials.

Received 11th December 2025,
Accepted 29th April 2026

DOI: 10.1039/d5dt02965a

rsc.li/dalton

Introduction

Among the various energy storage technologies, supercapacitors stand out due to their remarkably high-power density, rapid charge–discharge capability, and extended cycle life, making them promising candidates for next-generation energy storage applications.[1] Consequently, their utilization is continually expanding into diverse fields, including electric and hybrid vehicles, buses, trams, uninterruptible power supplies (UPS), temporary memory backup systems in computers, energy harvesting devices, solar energy systems, and wind turbines.[2,3]

The fundamental challenge in advancing supercapacitor technology is the development of effective electrode materials. Among various candidates, metal phthalocyanines (MPcs), organic semiconductors comprising four isoindole units coordinated around a central metal ion, are particularly noteworthy.[4,5] Their planar conjugated structure promotes efficient electron transport through π–π interactions, while strong adsorption ensures robust adherence to electrode surfaces. Additionally, the presence of 18-delocalized electrons in their macrocyclic structure facilitates charge transport and molecular stacking, further enhancing the electrochemical performance. MPcs demonstrate excellent thermal and chemical stability,[4,6] enabling their application under challenging conditions such as elevated temperatures and highly acidic or basic environments.

They can exist in covalent or electrovalent forms, with covalent MPcs exhibiting higher stability, capable of sublimation in a vacuum environment at 400–500 °C without structural decomposition.[7,8] Strong bonds between the metal centre and phthalocyanine ring, combined with aromatic stabilization, confer chemical resilience, resulting in minimal structural changes upon exposure to inorganic acids, except nitric acid (HNO_3). Some MPcs with an electrovalent character, containing alkali or alkaline metals, readily dissociate their metal ions upon exposure to acidic or aqueous media. However, copper-based MPcs employed in this study exhibit a covalent bonding character, providing greater chemical stability under similar conditions.[5,7]

[a]Ege University, Solar Energy Institute, Bornova, Bornova, 35100 İzmir, Türkiye
[b]Karadeniz Technical University, Faculty of Science, Department of Chemistry, Trabzon, Türkiye. E-mail: zekeriyab@ktu.edu.tr

The electronic properties and thus the electrochemical performance of MPcs significantly depend on the type of metal at their center. Divalent MPcs such as NiPc and CuPc exhibit a relatively low intrinsic conductivity ($\sim 10^{-12}$ S cm^{-1}),[9] necessitating their integration with conductive carbon materials, including carbon nanotubes, reduced graphene oxide (rGO), or porous carbons, to enhance their performance in practical applications.[10]

In this study, CuPc was functionalized with a (3,4,5-trimethoxybenzyl)oxy substituent to investigate how the substituent position, rather than substituent identity, affects electrochemical behaviour in supercapacitor electrodes. Two positional isomers, the peripheral (**TMe-Cu**) and non-peripheral (**n-TMe-Cu**) derivatives, were employed as a structurally controlled pair to clarify how molecular geometry influences electrode organization and charge-storage characteristics under identical testing conditions. While the electron-rich methoxy groups were expected to modulate the electronic structure and redox response of the CuPc framework, the positional arrangement of the substituent was anticipated to influence intermolecular packing, electrode microstructure, and the accessibility of electroactive domains. Structural, electrochemical, and kinetic analyses were therefore correlated to determine how peripheral and non-peripheral substitution patterns give rise to differences in interfacial charge-storage pathways, rate capability, and overall electrochemical utilization. The findings highlight the substituent geometry as an important molecular design parameter for CuPc-based organic supercapacitor electrodes.

Experimental

Materials and methods

The synthesis procedure of 3-[(3,4,5-trimethoxybenzyl)oxy] phthalonitrile (n-TMe-CN). TMe-OH (1 g, 5.05 mmol) was dissolved in 15 mL of anhydrous DMF. 3-Nitrophthalonitrile (872 mg, 5.05 mmol) was added. Then, dry K_2CO_3 (2.08 g, 15.15 mmol) was added in equal portions for 2 hours and the mixture was stirred at 60 °C for four days. Finally, the mixture was poured into iced water. **n-TMe-CN** was purified by column chromatography on aluminium oxide using $CHCl_3$ as a solvent. Yield: 450 mg (28%) m.p.: 170–171 °C. IR (ATR) ν/cm^{-1}: 3075 (Ar–H), 2941–2839 (Aliph. C–H), 2227 (C≡N), 1594, 1580, 1512, 1470, 1422, 1379, 1288, 1243, 1185, 1154, 1070, 1041, 993, 818, 733, 657, 626, 595. ^{1}H-NMR (400 MHz, DMSO-d_6), (δ): 7.85 (t, 1H, Ar–H), 7.73 (d, 1H, Ar–H), 7.67 (d, 1H, Ar–H), 6.80 (s, 2H, Ar–H), 5.27 (s, 2H, –CH_2-O), 3.76 (s, 6H, –O-CH_3), 3.65 (s, 3H, –O-CH_3). ^{13}C-NMR (100 MHz, DMSO-d_6), (δ): 161.12, 153.44, 137.79, 136.25, 131.31, 126.44, 119.54, 116.21, 115.84, 114.18, 105.59, 103.80, 71.59, 60.45, 56.31. MS (ESI), (m/z): 347.02 $[M + Na]^+$.

The synthesis procedure of peripherally and non-peripherally tetra-[(3,4,5-trimethoxybenzyl)oxy] group-substituted copper(II) phthalocyanines (TMe-Cu and n-TMe-Cu). A mixture of **TMe-CN** (100 mg, 0.3 mmol), **n-TMe-CN** (100 mg, 0.3 mmol), $CuCl_2$ (20 mg, 0.15 mmol), 1-pentanol (2 mL) and DBU (5 drops) was heated at 165 °C for 1 day. The product was precipitated with *n*-hexane. Then, **TMe-Cu** and **n-TMe-Cu** were purified by column chromatography on aluminium oxide using $CHCl_3$ as a solvent.

Copper(II) phthalocyanine (TMe-Cu). Yield: 75 mg (72%), m.p. >250 °C. IR (ATR), ν/cm^{-1}: 3071 (Ar–H), 2925–2846 (Aliph. C–H), 1590, 1504, 1454, 1419, 1374, 1329, 1224, 1118, 1088, 1055, 1000, 818, 744, 680. UV-Vis ($CHCl_3$) λ_{max} nm (log ε): 684 (4.93), 624 (4.54), 340 (4.73). MALDI-TOF-MS m/z: 1360.135 $[M]^+$.

Copper(II) phthalocyanine (n-TMe-Cu). Yield: 48 mg, 47%, m.p. >250 °C. IR (ATR) ν/cm^{-1}: 3061 (Ar–H), 2930–2831 (Aliph. C–H), 1588, 1501, 1454, 1417, 1328, 1230, 1121, 1084, 1005, 798, 739. UV-Vis ($CHCl_3$) λ_{max} nm (log ε): 710 (5.01), 646 (4.47), 327 (4.72). MALDI-TOF-MS m/z: 1360.135 $[M]^+$.

Electrode preparation

Three different components were used when preparing the material for the electrodes: Pc derivatives, carbon black (CB) as an additive to increase electrical conductivity and the surface area,[11] and PVDF-HFP as a binder.

The electrode base materials (TMeO-CuPc and n-TMeO-CuPc), carbon black (CB) and PVDF-HFP were mixed with acetone to obtain a homogeneous paste in a weight ratio of 80 : 15 : 5, respectively. The resulting paste was coated on a flexible graphite sheet used as a current collector and the electrodes were kept in a vacuum oven at 100 °C. The active electrode material covering an area of 1 cm^2 on each current collector is approximately 1 mg.

Electrochemical characterization

The electrochemical performance of the electrodes was tested with a three-electrode system. TMeO-CuPc and n-TMeO-CuPc were used as the working electrodes, Ag/AgCl was used as the reference electrode and Pt wire was used as the counter electrode. All measurements were performed using a 1 M H_2SO_4 electrolyte.

Cyclic voltammetry (CV), galvanostatic charge–discharge (GCD) and electrochemical impedance spectroscopy (EIS) analyses of the supercapacitors were performed using a CHI660E electrochemical workstation. Specific capacitance and energy and power densities were calculated from the measurements.

The gravimetric capacitance of SC cells was determined using the Galvanostatic Charge–Discharge (GCD) technique at various current densities. The gravimetric capacitance (C_s, F g^{-1}) obtained from GCD analysis was calculated for the three-electrode system using the following equation.[12]

$$C_s = \frac{I\Delta t}{m\Delta V} \quad (1)$$

where I is the constant current (A), m is the mass of the electrode material (g), Δt is the discharge time (s) and ΔV is the voltage change during the discharge process.

Electrochemical Impedance Spectroscopy (EIS) measurement was performed in the frequency range of 10 mHz–100

kHz to investigate the charge transfer between the electrode and electrolyte interface and ion diffusion across the electrode. The calculation of the total capacitance in the SC cell by EIS analysis is determined using the following formula.[13]

$$C = -\frac{1}{2\pi f Z''} \quad (2)$$

where Z'' represents the imaginary component of the impedance, while f represents the frequency in Hz of the applied AC signal.

Cyclic voltammetry (CV) studies on the SCs provide information on charge storage properties at electrode–electrolyte interfaces for different scan rates. The rectangular shape observed in the CV profiles refers to the capacitive behaviour of the cells, and the consistent maintenance of this shape at high scan rates indicates the high-rate capability of the cells. The following equation was used to calculate capacitance values from CV.[14]

$$C_s = \frac{\int IV\mathrm{d}V}{2mvk} \quad (3)$$

where m is the mass of the electrode material (g), $\frac{\int IV\mathrm{d}V}{2}$ is the charge area under the CV curve, v is the potential window (V) and k is the scan rate (V s^{-1}).

The energy density (E, Wh kg^{-1}) and power density (P, W kg^{-1}) for the SC cell were calculated using the following equations:

$$E = 0,5\frac{C_s(\Delta V)^2}{3,6} \quad (4)$$

$$P = \frac{E}{\Delta t_{\text{discharge}}}3600 \quad (5)$$

where C_s is the specific capacitance of the supercapacitor cell, V is the voltage change during the discharge process after the IR drop in the GCD curve and t is the discharge time.

Experimental

Synthesis and characterization of copper(II) phthalocyanines

The synthesis process of peripherally and non-peripherally tetra-[(3,4,5-trimethoxybenzyl)oxy] group-substituted copper(II) phthalocyanines (**TMe-Cu** and **n-TMe-Cu**) is shown in Fig. 1.

4-(3,4,5-Trimethoxybenzyloxy)phthalonitrile (**TMe-CN**) was synthesized according to the literature. In the IR spectrum of **n-TMe-CN**, C≡N stretching vibration was observed at 2227 cm^{-1}. In the ^{1}H-NMR spectrum of **n-TMe-CN**, aromatic protons appeared between 7.85 and 6.80 ppm. Also, –CH_2-O protons were observed at 5.27 ppm and –O-CH_3 protons were observed at 3.76 and 3.65 ppm. In the ^{13}C-NMR spectrum of **n-TMe-CN**, aromatic carbons were observed in the range of 161.12–103.80 ppm and aliphatic carbons were observed in the range of 71.59–56.31 ppm. The mass spectrum of **n-TMe-CN** showed a molecular ion peak at m/z 347.02 as $[M + Na]^+$. In the IR spectra of **TMe-Cu** and **n-TMe-Cu**, the absence of the C≡N

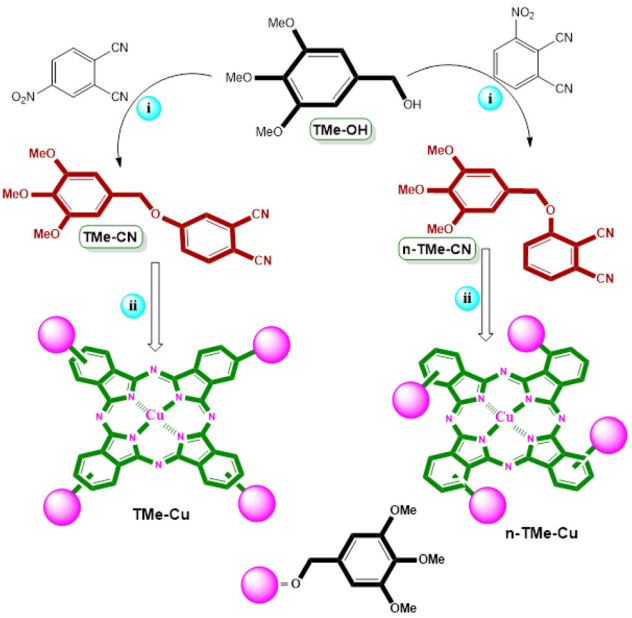

Fig. 1 The synthesis of **TMe-Cu** and **n-TMe-Cu**. (i) K_2CO_3, 60 °C, and DMF. (ii) $CuCl_2$, 1-pentanol, DBU, and 165 °C.

stretching vibrations at 2228 cm^{-1} and 2227 cm^{-1} supported the formation of metallo phthalocyanines. ^{1}H-NMR and ^{13}C-NMR measurements of **TMe-Cu** and **n-TMe-Cu** were excluded because of their paramagnetic properties.[15] The MALDI-TOF MS spectra of **TMe-Cu** and **n-TMe-Cu** showed molecular ion peaks at m/z 1360.13 as $[M]^+$ (**TMe-Cu**) (Fig. 2a) and 1360.13 as $[M]^+$ (**n-TMe-Cu**) (Fig. 2b).

The UV-visible spectra of **TMe-Cu** and **n-TMe-Cu** were recorded in $CHCl_3$ (Fig. 3). As shown in Fig. 3, **TMe-Cu** and **n-TMe-Cu** exhibited characteristic Q band absorptions at 684 nm and 710 nm, respectively, which were attributed to the π–π* transition of the phthalocyanine ring.[7] The other bands (B) in the UV region for **TMe-Cu** and **n-TMe-Cu** were observed at 340 nm and 327 nm, respectively, due to the transition from the deeper π-levels to the LUMO.

FT-IR spectroscopy was utilized to examine the chemical structure and substitution patterns of the synthesized phthalocyanine (Pc) derivatives (Fig. 4a). The characteristic vibrational peaks related to Pc macrocycles appear distinctly within the spectral region. Specifically, peaks observed at around 1605–1610 cm^{-1} correspond to the aromatic C=C stretching vibrations of the phthalocyanine ring. Additionally, prominent absorption bands at around 1480–1490 cm^{-1} can be attributed to aromatic C–N stretching vibrations typical of metal-coordinated phthalocyanines.[14,16] The bands in the 1240–1280 cm^{-1} region are associated with the aromatic ether (Ar–O–C) stretching vibrations originating from the (3,4,5-trimethoxybenzyl)oxy substituents.[6] Furthermore, the methoxy groups (–OCH_3) give rise to sharp and characteristic bands near 1025–1040 cm^{-1} due to C–O stretching vibrations.[17]

A comparative evaluation between the peripheral and non-peripheral derivatives reveals notable spectral shifts and inten-

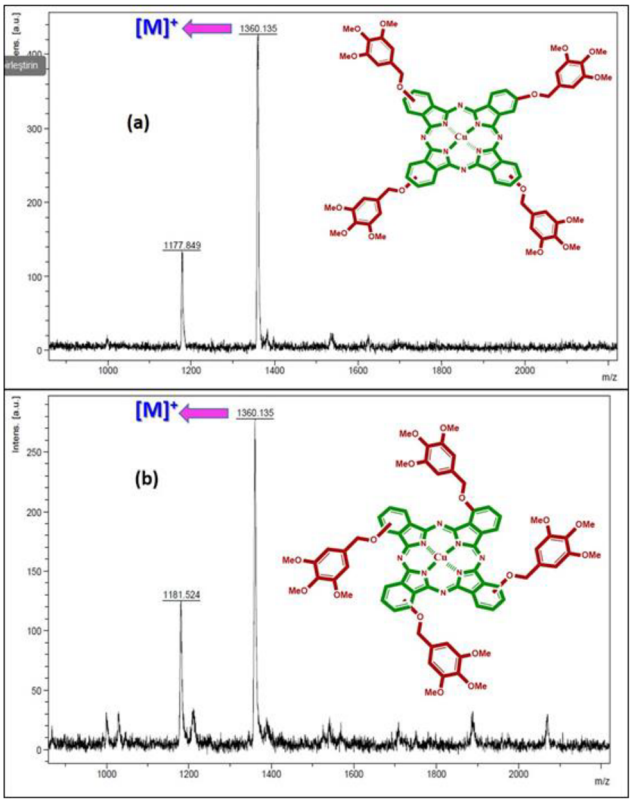

Fig. 2 MALDI-TOF MS spectra of (a) **TMe-Cu** and (b) **n-TMe-Cu**.

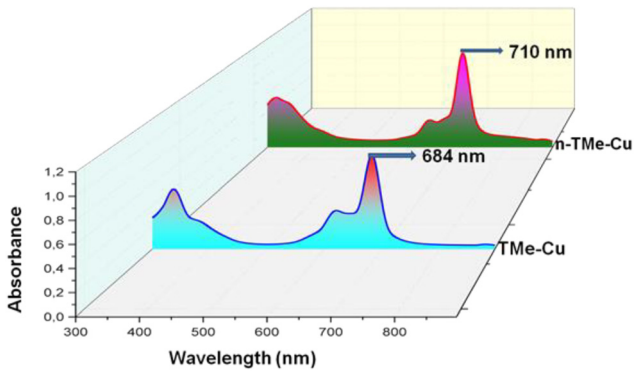

Fig. 3 UV-Vis spectra of **TMe-Cu** and **n-TMe-Cu** in $CHCl_3$.

sity variations. In the non-peripheral derivative (**n-TMe-Cu**), the vibration peaks appear slightly broader and shifted, indicating distortion in symmetry and enhanced intermolecular interactions due to increased steric hindrance. For instance, non-peripheral **n-TMe-Cu** exhibits broadened bands at around 1275 cm^{-1} and 1485 cm^{-1} compared to its peripheral counterpart **TMe-Cu**, suggesting greater disorder or intermolecular stacking differences.

The structural ordering and crystallinity of the Pc derivatives were further elucidated by XRD analysis (Fig. 4b). XRD diffractograms demonstrate characteristic broad peaks typically observed in molecularly aggregated, semi-crystalline

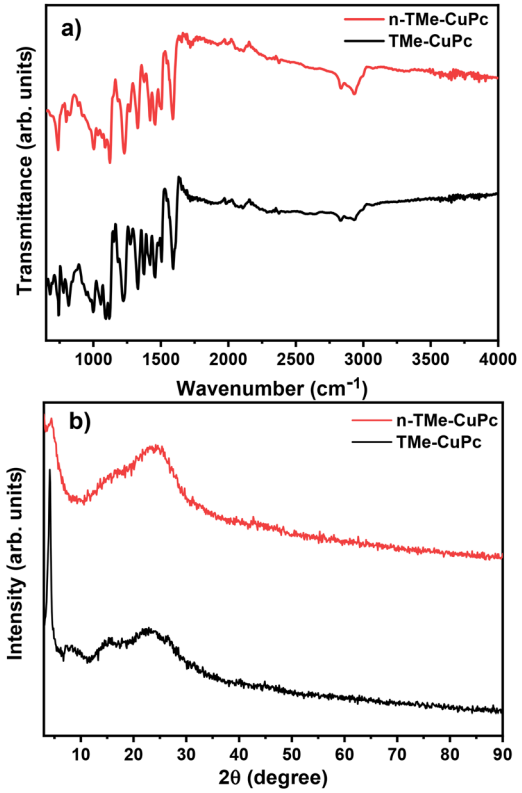

Fig. 4 (a) FTIR spectra of TMe-CuPc and n-TMe-CuPc. (b) XRD patterns of TMe-CuPc and n-TMe-CuPc.

phthalocyanines at around 20–30° and 40–45°. Notably, the **TMe-Cu** derivative exhibits a pronounced and relatively sharp diffraction peak below 5°, indicative of substantial molecular packing or self-assembly into ordered structures at the supramolecular scale.[18] Such a distinct feature is less pronounced in the non-peripheral analogues, where steric hindrance likely disrupts efficient π–π stacking. This finding correlates well with previously reported studies, where peripheral substituents significantly improved crystallinity due to more favourable molecular alignment.[7]

XPS was employed to investigate the elemental composition and chemical environment of the peripheral (**TMe-Cu**) and non-peripheral (**n-TMe-Cu**) copper phthalocyanine (CuPc) derivatives (Fig. 5). The analysis focused primarily on the Cu 2p region to evaluate the oxidation state and coordination environment of the central copper ion (Fig. 5a).

The high-resolution Cu 2p spectra of both derivatives exhibit prominent Cu $2p_{3/2}$ peaks located at around 934.2 eV and Cu $2p_{1/2}$ peaks near 953.8 eV, which are consistent with the presence of Cu(II) in a square-planar phthalocyanine coordination environment.[19] Additionally, the presence of satellite peaks in the 941–945 eV region confirms the d^9 electronic configuration typical of Cu^{2+} species.[20]

A comparison between the two substitution patterns reveals clear and meaningful differences. The Cu $2p_{3/2}$ peak of **n-TMe-Cu** appears slightly shifted to a higher binding energy

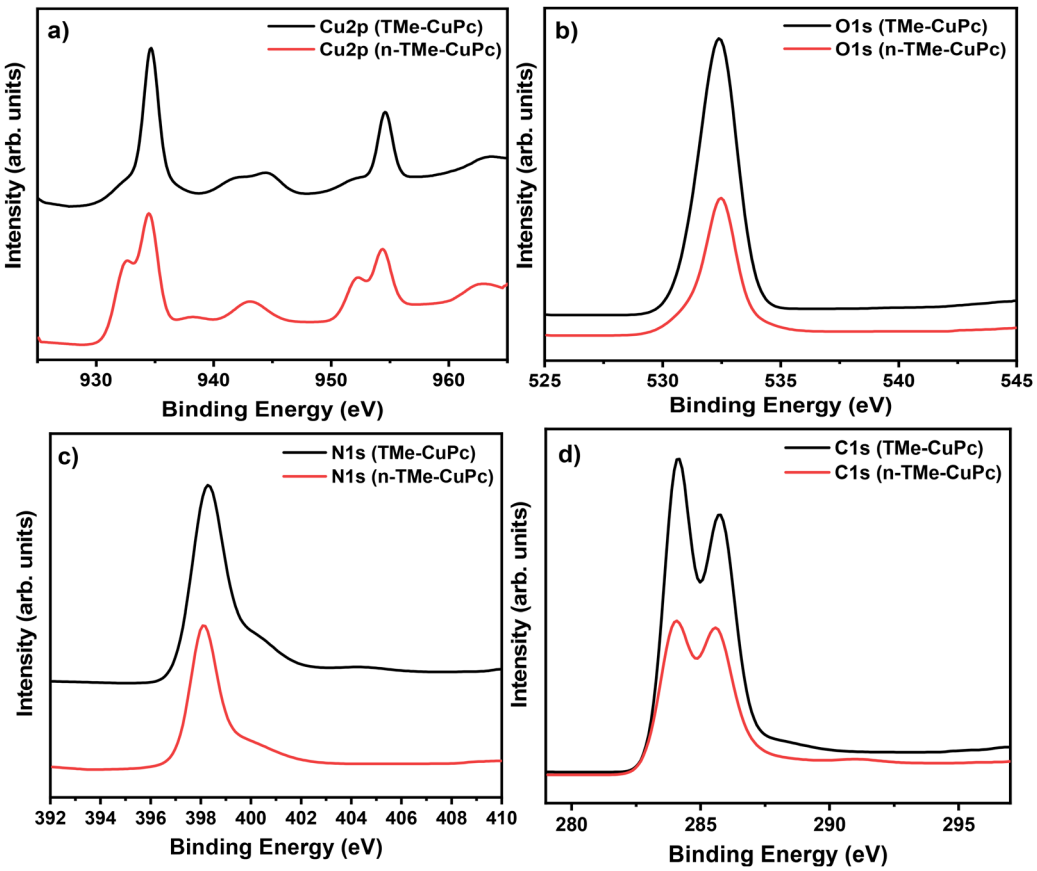

Fig. 5 XPS analyses of TMe-CuPc and n-TMe-CuPc. (a) Cu 2p, (b) O 1s, (c) N 1s, and (d) C 1s XPS spectra.

(~934.5 eV) compared to **TMe-Cu** (~934.2 eV), indicating a relatively more electron-deficient environment around the copper center in the non-peripheral derivative. This shift can be attributed to the increased steric hindrance and local asymmetry induced by non-peripheral substitution, which may reduce delocalization around the metal center and increase the localization of positive charge.[20] In contrast, **TMe-Cu** shows narrower peak widths and a slightly more symmetric Cu 2p profile, consistent with a more ordered molecular arrangement and stronger electronic delocalization afforded by the peripheral substituents.[21]

Furthermore, the intensity ratio between the main Cu $2p_{3/2}$ peak and its corresponding satellite features is slightly higher in **n-TMe-Cu**, suggesting a more pronounced shake-up effect and potentially greater contribution from localized d–d transitions. This observation supports the hypothesis that non-peripheral substitution introduces more heterogeneous electronic environments, which could enhance redox activity and facilitate pseudocapacitive behavior, as corroborated by CV and GCD analyses. The obtained results confirm that both derivatives retain Cu(II) oxidation states; however, they exhibited different behaviours in terms of the electronic environment, molecular symmetry, and delocalization characteristics, which in turn influence their electrochemical performance.

In addition to copper, the high-resolution XPS spectra of oxygen (O 1s), nitrogen (N 1s), and carbon (C 1s) provide further insight into the chemical environment of the macrocyclic framework and substituent groups (Fig. 5b–d). The N 1s region exhibits a primary peak near 399.5 eV, attributed to the isoindole nitrogen atoms in the phthalocyanine core, which is consistent across both derivatives.[20] A slight shoulder at higher binding energy (~401 eV) in **n-TMe-Cu** may reflect more heterogeneous hydrogen bonding or protonation effects, potentially due to increased structural disorder.

The C 1s spectra display characteristic components at ~284.6 eV (C–C/C═C), ~286.1 eV (C–O), and ~288.5 eV (O–C═O). Notably, the intensity of the C–O peak is higher in non-**TMe-Cu**, consistent with enhanced exposure of the (3,4,5-trimethoxybenzyl)oxy group and potentially leads greater electrolyte accessibility. The O 1s region shows peaks at around 531.5–533.0 eV, corresponding to contributions from the methoxy groups and possibly causes adsorbed water or oxygen species. Slight shifts to higher binding energy in the non-peripheral derivative again indicate a more electron-deficient local environment and support the interpretation of greater redox reactivity; however, differ clearly in terms of the electronic environment, molecular symmetry, and delocalization, which in turn influence their electrochemical performance.

Morphological characterization (SEM) of electrodes

The SEM micrographs (Fig. 6) reveal distinct surface textures for the electrodes prepared with two isomers at 20k× and 50k×. The electrode based on the peripheral derivative (**TMe-Cu**) exhibits a rough and heterogeneous texture composed of loosely connected aggregates, with visible gap regions and local discontinuities across the surface (Fig. 6a and c). In contrast, the non-peripheral derivative (**n-TMe-Cu**) forms a more continuous nanogranular film with compact granular domains and tighter interparticle contacts (Fig. 6b and d). At the examined magnifications, the superior electrochemical performance of **n-TMe-Cu** does not appear to arise from a more pronounced macroporous structure, but rather from the improved grain connectivity and better local film continuity. This morphological contrast suggests that the dominant difference lies not in the abundance of large open pores, but in how the grains pack, organize, and maintain interparticle contact within the electrode layer. Such differences are expected to influence interfacial electrochemical processes by modulating the accessibility to electroactive domains and the continuity of local ion/electron transport pathways. In this respect, the more coherent nanogranular texture of **n-TMe-Cu** is consistent with the higher surface-controlled contribution obtained from the kinetic analysis, whereas the rougher and more discontinuous morphology of **TMe-Cu** is more likely to contain transport-limited regions.[22,23]

Electrochemical characterization of electrodes

The electrochemical performance of the copper-based Pc derivatives as electrode materials was evaluated separately using a standard three-electrode configuration in a 1 M H_2SO_4 aqueous electrolyte. The working electrodes were prepared by casting a composite paste containing 80 wt% phthalocyanine derivative, 15 wt% conductive carbon black, and 5 wt% PVDF-HFP as a binder onto a conductive substrate, resulting in an effective area of 1 cm^2. These composition ratios were optimized based on our prior experience with Pc-based electrode materials.[11]

At a scan rate of 50 mV s^{-1}, gravimetric capacitance values calculated from the CV curves show a pronounced contrast between the two derivatives (Fig. 7a and b): **n-TMe-Cu** delivers 442.84 F g^{-1}, whereas **TMe-Cu** exhibits 79.82 F g^{-1}. This difference indicates that non-peripheral substitution enables a larger fraction of electroactive sites to participate under the applied timescale, yielding higher charge storage per unit mass in the same electrolyte and configuration.[24]

The scan-rate-dependent CVs (Fig. 7) provide additional kinetic insight beyond the single-scan comparison. As the scan rate increases from 10 to 100 mV s^{-1}, both electrodes show the expected increase in current response. However, their profile evolution differs markedly. For **n-TMe-Cu**, the voltammograms retain a broad, quasi-rectangular envelope with persistent faradaic distortion across the range, suggesting that a substantial portion of charge storage remains accessible within the shortened timescale and is governed by fast interfacial processes. In contrast, the **TMe-Cu** electrode shows a more pronounced distortion of the CV shape at higher scan rates, consistent with stronger polarization and a greater contribution from kinetically less accessible domains. At 50 mV s^{-1}, the capacitance derived from CV reaches 442.84 F g^{-1} for **n-TMe-Cu**, compared with 79.82 F g^{-1} for **TMe-Cu**, confirming the substantially higher electrochemical utilization of the non-peripheral derivative under identical conditions.

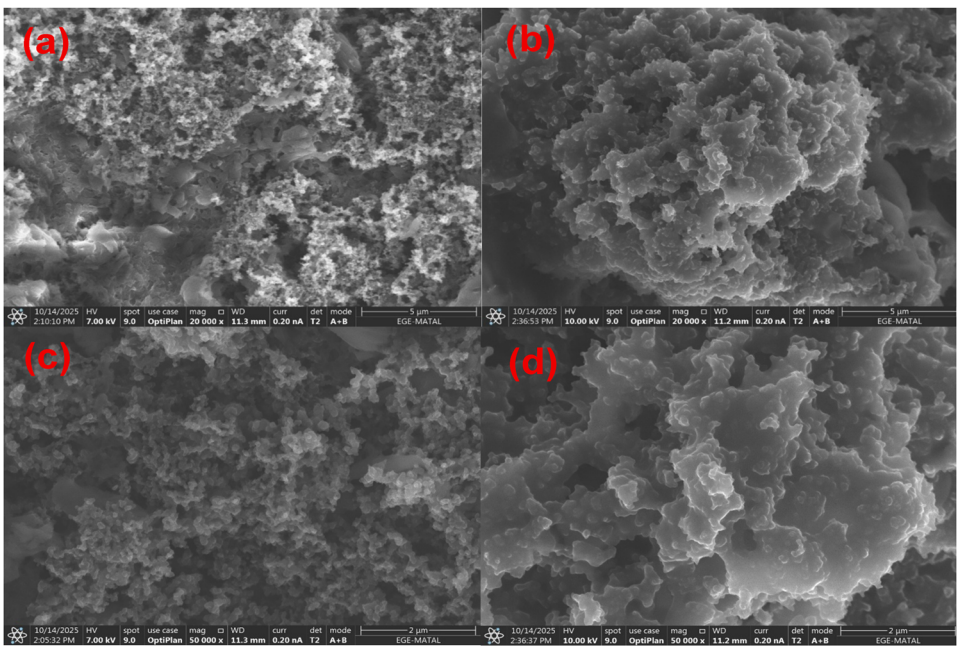

Fig. 6 SEM analyses: (a) 20k× and (c) 50k× images of TMe-CuPc; (b) 20k× and (d) 50k× images of n-TMe-CuPc.

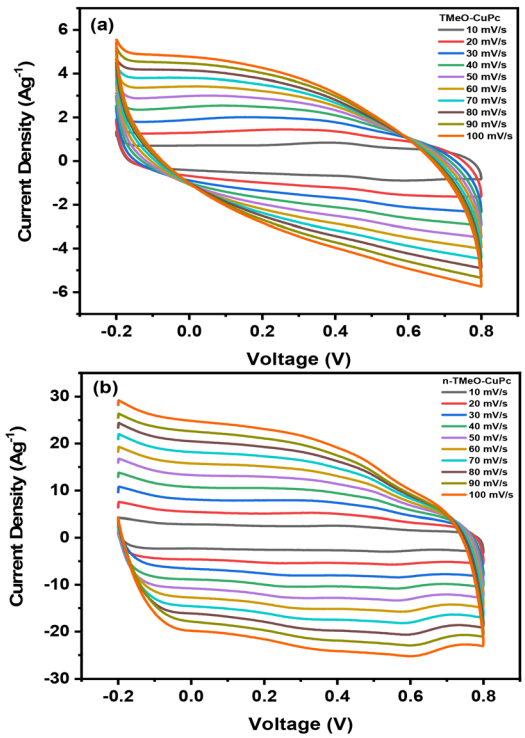

Fig. 7 CV curves of (a) TMe-CuPc and (b) n-TMe-CuPc at scan rates (10–100 mV s^{-1}).

To further quantify charge-storage kinetics, the dependence of current (i) on scan rate (v) was analysed using the power-law relationship.[25]

$$i(v) = av^b \quad (6)$$

Here, the exponent b provides a qualitative indicator of the kinetic regime: values close to 0.5 are characteristic of diffusion-limited processes, whereas values close to 1 indicate predominantly surface-controlled behaviour.[26] The b values extracted at 0.5 V are presented in Fig. 8a and c and indicate that both electrodes exhibit largely surface-controlled kinetics, with **n-TMe-Cu** displaying a pronounced surface-controlled contribution, consistent with pseudocapacitive-like behaviour.[26]

As a complementary assessment, Randles–Sevcik-type analysis was employed by examining the relationship between the redox current and $v^{1/2}$ (Fig. 8b and d). **TMe-Cu** shows clear linearity primarily for the anodic branch (R^2 = 0.9546), while the cathodic branch deviates from ideal diffusion scaling, indicating mixed kinetics. In contrast, **n-TMe-Cu** shows strong linearity for both anodic and cathodic branches (R^2 = 0.9984 and 0.9857, respectively), suggesting that diffusion-related transport contributes measurably to the overall response. Notably, this diffusion-related contribution can coexist with fast surface-controlled charge storage, consistent with the broad CV envelopes and the high capacitance observed for **n-TMe-Cu**.

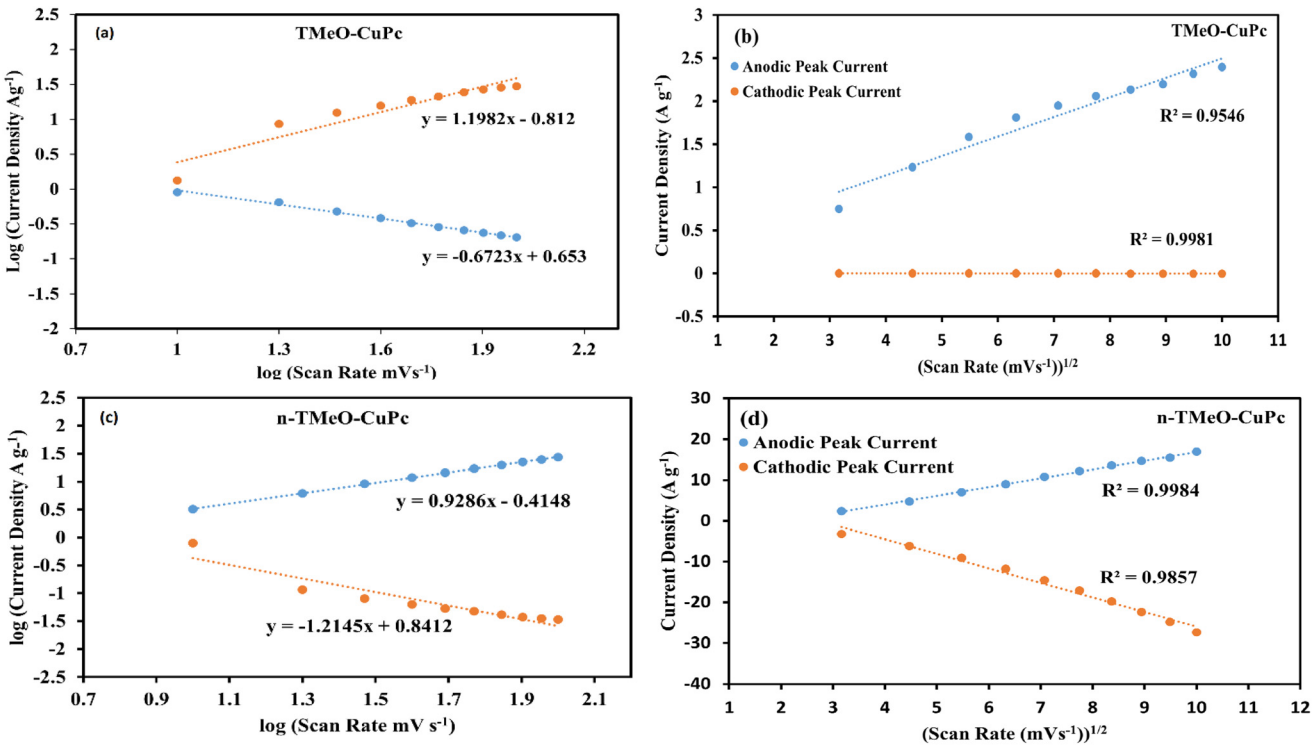

Fig. 8 Logarithm relationship between the anodic peak current and the scan rate (a) for TMe-CuPc and (c) for n-TMe-CuPc. Randles–Sevcik plots (linear curve of the anodic and cathodic current density *vs.* the square root of the scan rate) (b) for TMe-CuPc and (d) for n-TMe-CuPc.

To quantify the relative contributions of surface-controlled and diffusion-controlled charge storage, the Dunn method was applied:[26]

$$i_{\text{total}} = i_{\text{capacitive}} + i_{\text{diffusion}} \quad (7)$$

$$\frac{i(v)}{v^{1/2}} = k_1 v^{1/2} + k_2 \quad (8)$$

where $k_1 v$ corresponds to surface-controlled contributions and $k_2 v^{1/2}$ represents diffusion-limited contributions. Importantly, the surface-controlled (capacitive) term in the Dunn formalism is not restricted to pure electric double-layer charging; it also includes fast surface-confined faradaic (pseudocapacitive) processes that scale linearly with the scan rate. As shown in Fig. 9, **n-TMe-Cu** exhibits a consistently larger surface-controlled contribution than **TMe-Cu** across the entire scan-rate range. At 50 mV s^{-1}, the surface-controlled fraction reaches 83.5% for **n-TMe-Cu**, whereas **TMe-Cu** displays 49.2%. Across 10–100 mV s^{-1}, this contribution increases from 71.4% to 95.5% for **n-TMe-Cu**, while it increases from 31.7% to 68.6% for **TMe-Cu**. These results indicate that non-peripheral substitution enables a larger fraction of electroactive domains to participate through rapidly accessible interfacial pathways within the CV timescale. In contrast, the peripheral derivative shows a greater relative contribution from the transport-limited regions, particularly at lower scan rates. Combined with the SEM observations, the kinetic analysis indicates that the improved electrochemical performance of **n-TMe-Cu** arises primarily from a more favourable electrode microstructure, which promotes interfacial accessibility and more efficient charge-storage kinetics, rather than from a simple increase in macroporosity.

Electrochemical impedance spectroscopy (EIS) measurements were performed to evaluate the interfacial charge-transfer and transport characteristics of the CuPc-based electrodes (Fig. 10a and b). The Nyquist plots exhibit a clear high-frequency intercept on the real axis corresponding to the solution/bulk resistance, followed by a high-to-mid frequency interfacial response associated with charge-transfer and ion-transport processes in the electrode layer.[27] For clarity, the high-frequency region is shown as an inset in Fig. 10. The TMeO-CuPc electrode exhibits an R_b value of 1.34 Ω and an R_{ct} value of 0.46 Ω, whereas the corresponding values for n-TMeO-CuPc are 1.29 Ω and 0.59 Ω, respectively. These results indicate that the two electrodes exhibit comparable ohmic and interfacial resistance values, and therefore the superior electrochemical performance of n-TMeO-CuPc cannot be ascribed simply to a reduction in charge-transfer resistance.

More importantly, differences become evident in the overall impedance response and low-frequency behaviour, which reflect ion transport and electrochemical accessibility within the electrode architecture. In this respect, the EIS results are consistent with the scan-rate-dependent CV and Dunn analyses, indicating that the non-peripheral derivative enables

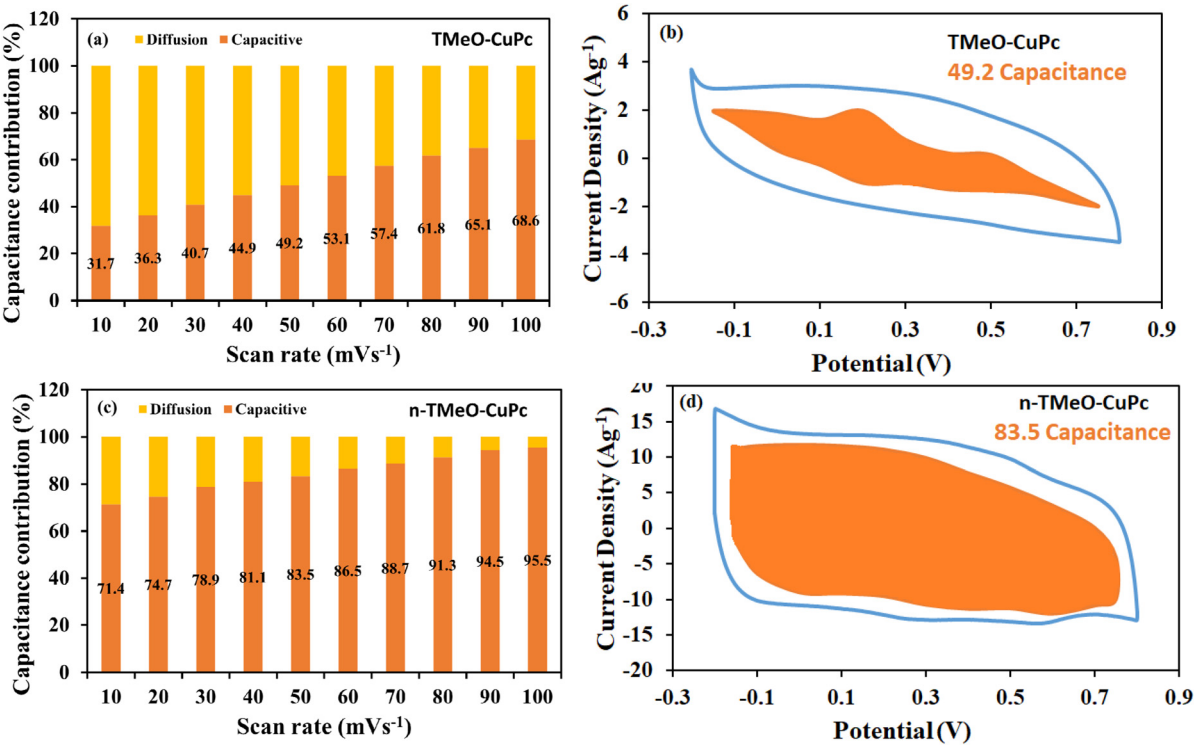

Fig. 9 Variation of the capacitive and diffusion charge distribution ratio at different scan rates (a) of TMe-CuPc and (c) n-TMe-CuPc. (b) Capacitive contribution of the TMe-CuPc electrode at a scan rate of 50 mV s^{-1}. (d) Capacitive contribution of the n-TMe-CuPc electrode at a scan rate of 50 mV s^{-1}.

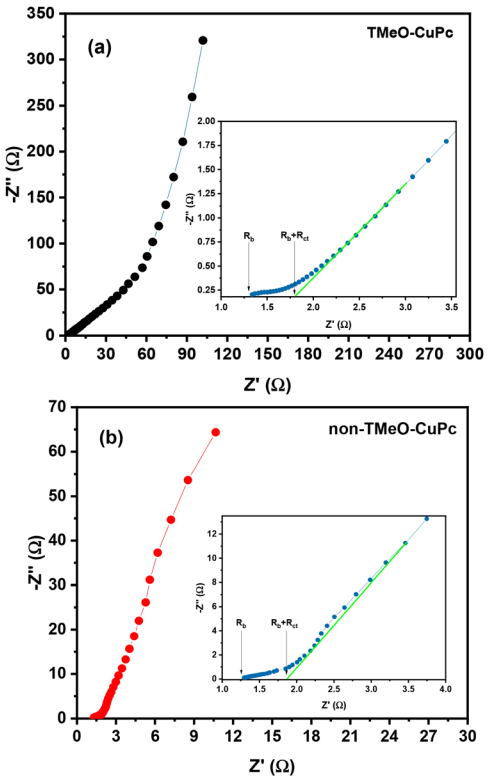

Fig. 10 Nyquist impedance spectra of the CuPc-based electrodes recorded in 1 M H_2SO_4 using a three-electrode configuration: (a) TMeO-CuPc and (b) n-TMeO-CuPc. For TMeO-CuPc, the high-frequency intercept corresponds to an R_b of 1.30 Ω and the arc diameter gives an R_{ct} of 0.50 Ω. For n-TMeO-CuPc, R_b is 1.25 Ω and R_{ct} is 0.60 Ω based on the same graphical evaluation. The insets show the high-frequency region.

more effective electrochemical utilization of accessible charge-storage domains despite not exhibiting a lower R_{ct} value. Accordingly, the performance advantage of n-TMeO-CuPc is more reasonably attributed to a more favourable electrode microstructure and interfacial accessibility than to a simple decrease in interfacial resistance.[28,29]

The charge–discharge behaviour of the CuPc-based electrodes was further examined using galvanostatic charge–discharge (GCD) measurements over a wide range of current densities (Fig. 11a and b), which provide insight into the rate capability and charge-storage dynamics of the peripheral (TMeO-CuPc) and non-peripheral (n-TMeO-CuPc) derivatives.

Across all current densities (0.2–2.0 A g^{-1}), n-TMeO-CuPc exhibits substantially longer discharge times than TMeO-CuPc, in agreement with its higher charge-storage capacity. At 1 A g^{-1}, n-TMeO-CuPc delivers a specific capacitance of 360 F g^{-1}, whereas TMeO-CuPc provides 67 F g^{-1}. With increasing current density, the capacitance decreases for both electrodes, reflecting the expected limitation of ion access and active-site utilization as the timescale becomes shorter; however, n-TMeO-CuPc maintains markedly higher capacitance across the entire range and retains over 333 F g^{-1} even at 2 A g^{-1} (Fig. 11c). This behaviour indicates superior rate capability of the non-peripheral derivative, consistent with a larger fraction of electrochemically accessible charge-storage sites and a more favourable kinetic balance under fast cycling conditions.[30] The literature on molecularly engineered phthalocyanine electrodes similarly emphasizes that electrode-level accessibility and utilization of redox-active domains strongly govern high-rate performance, particularly when transport limitations become pronounced.[31]

The GCD profiles also suggest distinct charge-storage characteristics. While TMeO-CuPc shows more nearly linear charge–discharge traces typical of predominantly capacitive behaviour, n-TMeO-CuPc exhibits more pronounced deviation from ideal linearity, consistent with additional pseudocapacitive/faradaic contributions superimposed on double-layer charging.[32]

Ragone analysis further highlights the performance gap: n-TMeO-CuPc achieves substantially higher energy density (up to 67 Wh kg^{-1} at a power density of 99.97 A g^{-1}) than TMeO-CuPc (<15 Wh kg^{-1}) while maintaining higher energy output at elevated power demands (99.66 A g^{-1}) (Fig. 11d). Overall, the GCD results corroborate the CV and kinetic analyses by demonstrating that non-peripheral substitution enhances effective electrochemical utilization and rate capability, rather than relying on a markedly reduced interfacial resistance.

The cycling stability of the electrodes was evaluated by galvanostatic charge–discharge measurements for 5000 cycles at a relatively high current density of 2 A g^{-1} under ambient atmosphere (Fig. 12). The n-TMeO-CuPc electrode delivers an initial specific capacitance of 358.3 F g^{-1} and maintains 286.3 F g^{-1} after prolonged operation, corresponding to 80% capacitance retention. A comparable retention ratio is observed for TMeO-CuPc, which sustains 44.4 F g^{-1} from an initial value of 60 F g^{-1}. These results demonstrate that both electrodes exhibit robust capacitive behaviour even at a high current load and without any special environmental control, while the non-peripherally substituted n-TMeO-CuPc (80%) electrode consistently provides several-fold higher capacitance than its peripheral analogue, confirming its clear advantage for practical supercapacitor applications. As summarized in Table S1, the present CuPc system performs competitively relative to representative phthalocyanine-based supercapacitor electrodes, while providing a clearer molecular-level structure–property correlation than most composite or device-oriented architectures. The **n-TMe-Cu** electrode delivers 360 F g^{-1} at 1 A g^{-1} with 80% capacitance retention after 5000 cycles, placing it above several previously reported CuPc- and MPc-based electrodes evaluated under comparable three-electrode conditions. While some rGO- or CNT-containing hybrid systems achieve higher absolute capacitance or device-level energy density, those enhancements are often coupled to additional contributions from conductive scaffolds and composite-engineering effects. In contrast, the present work evaluates a structurally controlled pair of positional isomers within the same CuPc framework, allowing the influence of substituent geometry on electrode microstructure, interfacial accessibility, and charge-

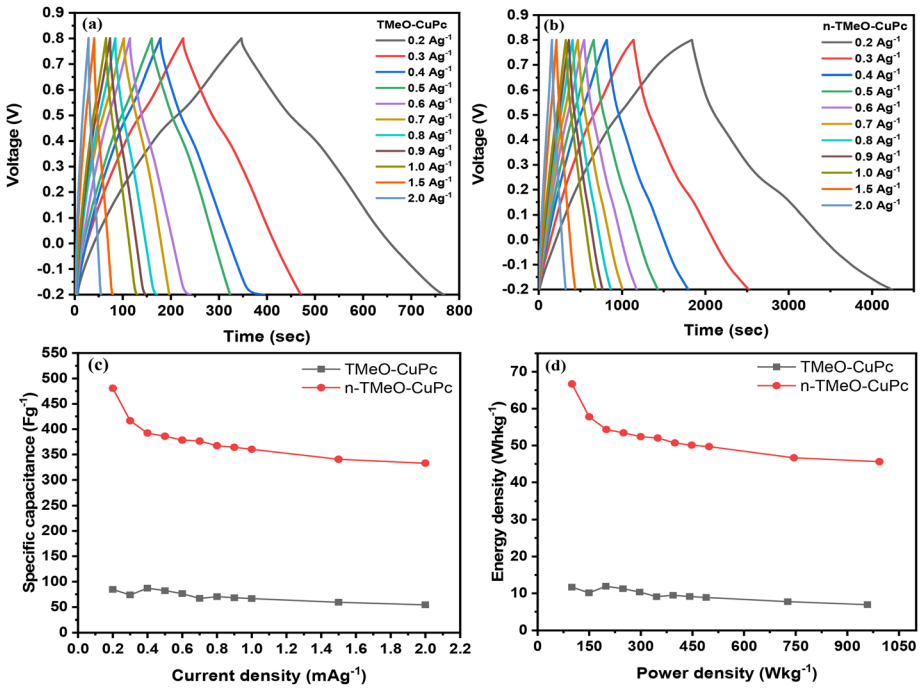

Fig. 11 CDC curves of (a) TMe-CuPc and (b) n-TMe-CuPc at different current densities. (c) Specific capacity as a function of different current densities (0.2–2.0 A g^{-1}) (calculated from the CDC curves). (d) Comparison of the energy density and power density calculated from the CDC curves of TMe-CuPc and n-TMe-CuPc at various current distributions (Ragone plot).

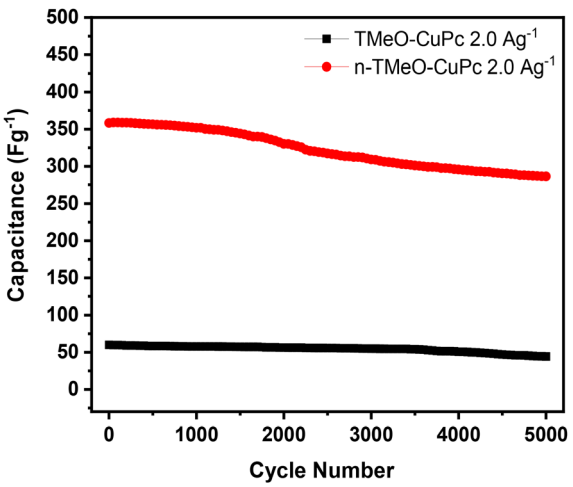

Fig. 12 Cycling stability of the CuPc-based electrodes evaluated by galvanostatic charge–discharge (GCD) at a current density of 2 A g^{-1} over 5000 cycles in 1 M H_2SO_4 using a three-electrode configuration: (a) peripheral derivative (TMeO-CuPc) and (b) non-peripheral derivative (non-TMeO-CuPc). The plots show the capacitance retention as a function of the cycle number, highlighting the long-term charge–discharge durability under repeated high-rate cycling.

storage kinetics to be identified more directly. The results therefore highlight that the importance of this system lies not only in its electrochemical performance but also in demonstrating how non-peripheral substitution can translate into a more coherent electrode morphology and a larger surface-controlled contribution to capacitive charge storage.[33–35]

Conclusions

In this work, two structurally distinct copper phthalocyanine derivatives, peripherally substituted (TMeO-CuPc) and non-peripherally substituted (n-TMeO-CuPc), were synthesized using a (3,4,5-trimethoxybenzyl)oxy functional group and systematically evaluated as supercapacitor electrode materials. Structural characterization by MALDI-TOF MS, FT-IR, UV–vis, XRD, and XPS analyses confirmed the expected substitution-dependent differences in molecular ordering. Electrochemical evaluation by cyclic voltammetry, galvanostatic charge–discharge, electrochemical impedance spectroscopy, and scan-rate-dependent kinetic analyses revealed a pronounced performance advantage for **n-TMe-Cu**, which delivered a specific capacitance of up to 360 F g^{-1} at 1 A g^{-1} and retained 80% of its initial capacitance after 5000 charge–discharge cycles. Kinetic analysis showed that **n-TMe-Cu** exhibits a consistently higher surface-controlled contribution than **TMe-Cu**, indicating that a larger fraction of charge storage proceeds through rapidly accessible interfacial pathways. When interpreted together with the SEM observations, these findings suggest that the superior performance of the non-peripheral derivative is associated not with a simple increase in macroporosity or a lower charge-transfer resistance but with a more favourable electrode microstructure that improves interfacial accessibility

and electrochemical utilization. Overall, the results demonstrate that the substituent position plays a decisive role in regulating electrode organization, charge-storage kinetics, and rate capability in CuPc-based electrodes. This work therefore identifies substituent geometry as an effective molecular design parameter for the development of high-performance organic supercapacitor materials.

Author contributions

S. S. G.: conceptualization, methodology, formal analysis, investigation, and writing – original draft. B. A. Ö.: methodology, visualization, investigation, formal analysis, and writing –original draft. D. Ş.: investigation, visualization, and writing – editing. G. Y.: formal analysis, visualization, and writing – editing, B. T. E.: formal analysis, methodology, and writing – review and editing. B. G.: resources, methodology, writing – review and editing, and supervision. Z. B.: resources, conceptualization, writing – review and editing, and supervision. All authors have read and agreed to the submitted version of the manuscript.

Conflicts of interest

There are no conflicts to declare.

Data availability

The data supporting this article have been included as part of the supplementary information (SI). Supplementary information is available. See DOI: https://doi.org/10.1039/d5dt02965a.

Acknowledgements

Damla Sahin and Gulsah Yılmazwas were supported by TUBITAK with a scholarship under the 2211-C National PhD Scholarship Program in the Priority Fields in Science and Technology. Burak Gultekin would like to acknowledge the Presidency of Turkey, Department of Strategy and Budget for infrastructure and some of the consumables (project #: 2016 K121200—16DPT002).

References

1 P. Simon and Y. Gogotsi, *Nat. Mater.*, 2008, **7**, 845–854.
2 J. R. Miller and P. Simon, *Science*, 2008, **321**, 651–652.
3 S. Chakraborty and N. L. Mary, *J. Electrochem. Soc.*, 2022, **169**, 020552.
4 G. Denes, *J. Am. Chem. Soc.*, 1998, **120**, 241–242.
5 T. Shimizu, K. Wakamatsu, Y. Yamada, Y. Toyoda, S. Akine, K. Yoza and H. Yoshikawa, *ACS Appl. Mater. Interfaces*, 2021, **13**, 40612–40617.
6 D. Gounden, N. Nombona and W. E. van Zyl, *Coord. Chem. Rev.*, 2020, **420**, 213359.
7 C. G. Claessens, U. Hahn and T. Torres, *Chem. Rec.*, 2008, **8**, 75–97.
8 S. E. Dyusenova, D. D. Klyamer, A. S. Sukhikh, I. M. Shchudlo, S. Y. Taskaev, T. V. Basova and S. A. Gromilov, *J. Struct. Chem.*, 2023, **64**, 337–346.
9 S. Ambily and C. S. Menon, *Solid State Commun.*, 1995, **94**, 485–487.
10 O. Gorduk, S. Gorduk, M. Gencten, M. Sahin and Y. Sahin, *Int. J. Energy Res.*, 2020, **44**, 9093–9111.
11 S. Siyahjani, S. Oner, H. Diker, B. Gultekin and C. Varlikli, *J. Power Sources*, 2020, **467**, 228353.
12 Y. Zheng, Q. Liu, X. Guan, Y. Liu, S. Nie and Y. Wang, *Micromachines*, 2022, **13**, 1747.
13 K. Sheng, Y. Sun, C. Li, W. Yuan and G. Shi, *Sci. Rep.*, 2012, **2**, 247.
14 M. Salih Ağrtaş, B. Cabir and S. Özdemir, *Dyes Pigm.*, 2013, **96**, 152–157.
15 H. Fazlı, Z. Biyiklioglu, E. T. Saka, Ö. Kesmez and F. Demir, *Appl. Organomet. Chem.*, 2025, **39**, e70352.
16 V. Balachandran, V. Karpagam, G. Santhi, B. Revathi, G. Ilango and M. Kavimani, *Spectrochim. Acta, Part A*, 2015, **137**, 165–175.
17 D. Klyamer, A. Sukhikh, N. Nikolaeva, N. Morozova and T. Basova, *Sensors*, 2020, **20**, 1893.
18 M. Yokota, K. Fujii, M. Ishigo, K. Sasaki, H. Kato and N. Doki, *Adv. Chem. Eng. Sci.*, 2016, **06**, 82–86.
19 Z. Chen, X. Wang, W. Lang and D. Qi, *RSC Adv.*, 2019, **9**, 32490–32498.
20 D. G. De Oteyza, A. El-Sayed, J. M. Garcia-Lastra, E. Goiri, T. N. Krauss, A. Turak, E. Barrena, H. Dosch, J. Zegenhagen, A. Rubio, Y. Wakayama and J. E. Ortega, *J. Chem. Phys.*, 2010, **133**, 214703.
21 M. Isobe, F. Abe, S. Takagi and K. Kanai, *ACS Omega*, 2024, **9**, 32133–32143.
22 J. Chmiola, C. Largeot, P. L. Taberna, P. Simon and Y. Gogotsi, *Angew. Chem., Int. Ed.*, 2008, **47**, 3392–3395.
23 E. Raymundo-Piñero, K. Kierzek, J. Machnikowski and F. Béguin, *Carbon*, 2006, **44**, 2498–2507.
24 W. Zhang, Y. Yang, M. Ravi, L. Kong, L. Kang and F. Ran, *Electrochim. Acta*, 2019, **306**, 113–121.
25 J. Liu, J. Wang, C. Xu, H. Jiang, C. Li, L. Zhang, J. Lin and Z. X. Shen, *Adv. Sci.*, 2018, **5**, 1700322.
26 B. Dunn, H. Kamath and J. M. Tarascon, *Science*, 2011, **334**, 928–935.
27 N. F. Atta, *Eur. Polym. J.*, 2005, **41**, 3018–3025.
28 E. A. Al-Harthi, M. Imran, M. S. Rashid, A. Asghar, H. R. Khan, M. A. Shakera, A. A. Yakout and A. Khan, *Inorg. Chem. Commun.*, 2025, **178**, 114616.
29 J. Mao, J. Iocozzia, J. Huang, K. Meng, Y. Lai and Z. Lin, *Graphene aerogels for efficient energy storage and conversion*, The Royal Society of Chemistry, 2018, DOI: 10.1039/c7ee03031b.

30 V. Ramkumar, M. Muniyandi, A. Thirumurugan, G. Sandoval-Hevia, M. Santhamoorthy and S. C. Kim, *J. Alloys Compd.*, 2025, **1042**, 184037.
31 A. A. Özen, T. Göktürk, T. Hökelek, R. Güp, C. Topkaya, A. B. Bilge and S. Aslan, *ACS Omega*, 2025, **10**, 41595–41607.
32 Y. Wang, M. Li, R. Ramachandran, H. Shan, Q. Chen, A. Luo, F. Wang and Z. X. Xu, *J. Energy Chem.*, 2023, **76**, 214–225.
33 F. Qi, Y. Wang, J. Xu, X. Wang, J. Wang, H. Shan, M. Li and J. Xu, *Synth. Met.*, 2023, **293**, 117284.
34 M. Wang, H. Shi, P. Zhang, Z. Liao, M. Wang, H. Zhong, F. Schwotzer, A. S. Nia, E. Zschech, S. Zhou, S. Kaskel, R. Dong and X. Feng, *Adv. Funct. Mater.*, 2020, **30**, 2002664.
35 R. Ganesan and J. R. Xavier, *Synth. Met.*, 2026, **317**, 118065.